Strain tuning of optoelectronic properties of covalent organic framework bilayers and heterostructures

M. Alihosseini and M. Neek-Amal [*]

Department of Physics, Shahid Rajaee Teacher Training University, 16875-163 Lavizan, Tehran, Iran

Heterostructures composed of two-dimensional materials have gained significant attention due to their unique properties and potential applications in various fields. Covalent organic frameworks (COFs) represent a novel class of organic porous materials that have shown promise in gas storage, catalysis, and optoelectronics. In this paper, we present a first-principles study of the optoelectronic properties of bilayers and heterostructures of C_6N_6 and B_6O_6 COFs, including excitonic effects within the G_0W_0-BSE approach and the effects of van der Waals corrections. Our study shows that the energetically favorable configuration is AC-stacking, where the upper pore is covered by the C-N (B-O) ring of the bottom layer. We also found that the AC-stacking C_6N_6/B_6O_6 heterostructure exhibits a surface buckling of 0.55 Å and an intrinsic type II band alignment, resulting in a redshift in optical absorption. The calculated band edge alignments for C_6N_6 and B_6O_6 monolayers and heterostructures using the HSE06 hybrid functional affirm their suitability for the photocatalytic splitting of water. Furthermore, we investigated the impact of strain on the band gap and demonstrated that increasing tensile strain leads to a decrease in the distance between the two layers, causing an increase in the electronic band gap and optical gap. These results provide a solid theoretical foundation for future experimental investigations and suggest potential applications in optoelectronic devices. Overall, our study sheds light on the optoelectronic properties of COF heterostructures and highlights their potential for use in a range of important applications.

I. INTRODUCTION

Porous organic frameworks (POFs) composed of organic monomers made of light, nonmetallic elements (such as C, H, N, B, O, and Si) joined by strong covalent bonds are a novel class of porous materials [1,2]. Porous materials have received a lot of attention recently because of their distinctive qualities of high stability, large surface area, and wide range of applications in ion separation, gas sorption, water purification, energy storage, catalysis, and drug delivery [3–13]. There are many different kinds of POFs, such as conjugated microporous polymers (CMPs), porous aromatic frameworks (PAFs), polymers of intrinsic microporosity (PIMs), covalent organic frameworks (COFs), and hyper-cross-linked polymers (HCPs) [14–23]. In fact, COFs are a type of predictable crystal structure that possess intrinsic porosity and thermal stability, making them suitable for molecular transport, drug delivery, and energy storage applications. A variety of crystalline COFs have been developed with covalent linkages such as B-O (boronate ester, boroxine, borosilicate, and spiroborate), B-N (borazine), C-C, C-N (imine, hydrazone, imide, ketoenamine, azine, triazine, melamine, amide, phenazine, squaraine, and viologen), and N-N (azodioxide) according to recent studies [24–26].

By varying the number of degrees of freedom, different kinds of COF structures with various chemical and electrical characteristics can be developed [27–30]. Addi-

tionally, atom-thick two-dimensional (2D) COFs have been produced experimentally and have demonstrated potential in semiconductor applications [31–33]. The high electrical properties and charge transport of 2D COFs, when compared to microporous metal-organic frameworks (MOFs) or porous coordinated polymers (PCPs), have garnered considerable attention [34,35]. A heptazine-based COF was synthesized using the Schiff-base reaction and has shown highly efficient photocatalytic H_2O_2 production, with enhanced light absorption and charge separation [36].

The structural and electronic properties of COFs have been extensively studied in theoretical and experimental investigations thus far [28,31,37–40]. For instance, Zhu *et al.* systematically investigated the effect of COF system size on the electronic band gap using density functional theory calculations [28]. The electronic band gaps are reduced dramatically when the COF's branches are extended, and it was also demonstrated that the electronic characteristics of COFs are not significantly changed by the graphene substrate [28].

Using density functional theory and many-body GW calculations, Liang *et al.* studied the structural and electronic properties of two types of 2D monolayer structures of COFs belonging to two major families: thiophene-based COF-*n* (T-COF-*n*) and tetrakis (4-aminophenyl) porphyrin-*x* (TAPP-*x*). Their findings indicate that T-COF-*n* systems form flat structures, while the TAPP-*x* systems can have non-negligible buckling due to the out-of-plane rotation of the phenyl rings. The obtained electronic band gaps of the T-COF-1, -2, -3, and -4 systems reveal that they are wide band-gap semiconductors and are not greatly impacted by the change in chain molecules

*mehdi.neekamal@gmail.com

[41]. Additionally, the presence of the substrate causes band-gap decreases in the systems due to the polarization effects of the substrate, and the reduction in the gap is highly dependent on the substrate's dielectric constant [41]. Another study has reported that the porous 2D C_2N (h2D-C_2N) crystal is a direct-gap semiconductor COF with electronic band gaps of about 1.71 and 2.44 eV obtained at the GGA-PBE and HSE06 hybrid functional levels [42,43]. First-principles analysis of electron transport has demonstrated that band transport is operational in the h2D-C_2N system for both low and high temperatures [43]. Moreover, applying biaxial strains can successfully tune the electronic and optical characteristics of h2D-C_2N [44].

In particular, a novel 2D porous graphitic carbon nitride (C_6N_6) has been experimentally and theoretically studied in recent years, exhibiting remarkable thermodynamic and kinetic stability [45–50]. Compared to C_3N_4, s-triazines in C_6N_6 are connected by C-C bonds without requiring extra nitrogen atoms. Direct Δ values of freestanding C_6N_6 have been calculated to be 1.54, 2.89, and 3.18 eV using PBE, HSE03, and HSE06 hybrid functional calculations, respectively [47]. The thermodynamic and kinetic stability of this novel 2D porous graphitic carbon nitride has been experimentally and theoretically studied in recent years [45–50]. The opening of the band gap due to spin-orbit coupling (SOC) suggests that C_6N_6 may exhibit the quantum spin Hall effect (QSHE) at temperatures below 95 K [48]. Moreover, the boroxine-based COF (B_6O_6) is another newly synthesized 2D porous material that exhibits high thermal stability and offers a range of optoelectronic and gas-sensing applications [51–55]. This substance has an entirely planar structure with indirect electronic Δ values of 3.80 and 5.3 eV obtained at the vdW-DF and HSE levels, respectively [52].

There are various techniques developed to modify the characteristics of 2D materials, including applying an external electric field, inducing uniaxial and biaxial strains, and stacking monolayers via van der Waals (vdW) interactions [56–64]. The interface of two monolayers (MLs) is stabilized by weak vdW forces, which preserve the intrinsic properties of each layer in HTS [63,65]. While several studies have focused on the electronic and optical properties of various vdW HTS containing C_6N_6, such as C_6N_6/graphene, C_6N_6/C_2N, C_6N_6/C_3N_4, and C_6N_6/InP [66–70], the C_6N_6/B_6O_6 HTS have not yet been investigated.

In this paper, we use *ab initio* calculations to investigate the electronic properties of C_6N_6 and B_6O_6 bilayers (BLs) and two different stacking configurations of C_6N_6/B_6O_6 HTS. Furthermore, we analyze the optical properties of the most stable configuration of the C_6N_6/B_6O_6 heterostructure and study the effect of strain on the electronic properties of this system. Our study aims to provide insights into the potential applications of these materials and their HTS in optoelectronic and sensing devices.

II. COMPUTATIONAL DETAILS

The first-principles calculations in this study are performed using the generalized gradient approximation (GGA) with the Perdew-Burke-Ernzerh (PBE) exchange-correlation functional, which is implemented in the Quantum ESPRESSO

(QE) computational package [71,72]. The interaction between the ion cores and valence electrons is simulated using ultrasoft pseudopotentials. To study the effects of nonlocal correlations, the van der Waals density functional (vdW-DF) is employed [73,74]. The cutoff values for plane-wave kinetic energy and charge density are determined to be 60 Ry and 600 Ry, respectively, after conducting a convergence test. Additionally, the total energy convergence threshold is set to 10^{-6} eV. The accuracy of forces on each atom is calculated to be approximately 0.1 mRy/bohr for relaxing the cell parameters and atomic positions. A $6 \times 6 \times 1$ k-point grid is selected for the unit cell of MLs and HTS. For non-self-consistent calculations in partial density of states (PDOS) analysis, a $48 \times 48 \times 1$ Monkhorst-Pack mesh of k points is chosen [75]. We also employed a Gaussian smearing width of 0.2 eV for the PDOS calculations. The 2D HTS are modeled as periodic slabs with a sufficiently large vacuum layer of 20 Å to eliminate artificial interaction effects between adjacent layers. Additionally, the computations are also carried out using the Heyd-Scuseria-Ernzerhof (HSE06) method with optimized norm-conserving Vanderbilt (ONCV) pseudopotentials to obtain more precise electronic properties [76–78]. To consider the effects of many-body interactions, we utilized a generalized plasmon-pole model, which gives rise to quasiparticle (QP) energies through a single-shot GW (G_0W_0) approach, using initial results from DFT calculations [79]. The ONCV pseudopotentials are used to derive quasiparticle energies and optical characteristics. A box-shape truncated Coulomb interaction with a dimension of at least 17 Å in the z direction is employed to eliminate the long-range nature of the Coulomb interaction [80]. The parameters employed in our calculations include a wave-function cutoff of 60 Ry, a $16 \times 16 \times 1$ k-point grid, within an accuracy of approximately 0.1 eV, a 10 Ry cutoff for the dielectric matrix, and consideration of 200 bands. Through the solution of the Bethe-Salpeter equation (BSE) and the incorporation of excitonic electron-hole interactions, the optical absorption spectra were obtained [81,82]. We considered the 10 highest valence bands and the 10 lowest conduction bands for BSE calculations. The calculations for both GW and BSE are conducted using the Yambo package [83]. Born-Oppenheimer AIMD simulations with 1000 steps (about 1.145 ps) are performed to simulate the canonical ensemble (NVT) at a temperature of 300 K. The charge transfer between layers is calculated using Bader charge analysis [84].

III. RESULTS AND DISCUSSION

The optimized geometries of the C_6N_6 and B_6O_6 MLs are shown in Figs. S1(a) and S1(b) in the Supplemental Material [85]. Both C_6N_6 and B_6O_6 possess planar hexagonal structures with lattice constants of 7.12 and 7.83 Å, respectively, which are consistent with previous studies [47,49,52,53]. A unit cell of each monolayer contains six C (B) atoms and six N (O) atoms with a uniform pore in the C_6N_6 (B_6O_6) layer. The phonon calculations conducted earlier demonstrate the systems' geometrical stability [53,86]. The optimized bond lengths and pore diameters (d_{N-N} and d_{O-O}) are listed in Table I.

TABLE I. Structural and electronic parameters of C_6N_6/B_6O_6 monolayers (ML), bilayers (BL), and heterostructures (HTS) including the PBE-GGA electronic band gap [Δ(GGA)], lattice constant (a), buckling of layers (δ), interlayer distance between two layers (h), adhesion energy (E_a), bond length between C–C atoms (d_{C-C}), bond length between C–N atoms (d_{C-N}), pore diameter of C_6N_6 (d_{N-N}), bond length between B–B atoms (d_{B-B}), bond length between B–O atoms (d_{B-O}), and pore diameter of B_6O_6 (d_{O-O}). Values for [Δ(GGA)] and E_a are in eV, and all structural parameters are in Å.

	Structure	Δ(GGA)	a	δ	h	E_a	d_{C-C}	d_{C-N}	d_{N-N}	d_{B-B}	d_{B-O}	d_{O-O}
ML	C_6N_6	1.68 (D)	7.12	0	—	—	1.51	1.34	5.46	—	—	—
	B_6O_6	3.79 (I)	7.83	0	—	—	—	—	—	1.72	1.39	6.29
BL	C_6N_6 (AA)	1.45 (D)	7.12	0	3.79	−0.35	1.50	1.34	5.46	—	—	—
	C_6N_6 (AB)	1.62 (D)	7.12	0	3.59	−0.50	1.50	1.34	5.46	—	—	—
	C_6N_6 (AC)	1.63 (I)	7.12	0	3.33	−0.69	1.50	1.34	5.46	—	—	—
	B_6O_6 (AA)	3.42 (I)	7.83	0	3.86	−0.28	—	—	—	1.71	1.39	6.29
	B_6O_6 (AB)	3.64 (D)	7.83	0	3.39	−0.44	—	—	—	1.72	1.39	6.30
	B_6O_6 (AC)	3.76 (I)	7.83	0	3.19	−0.61	—	—	—	1.71	1.39	6.29
HTS	C_6N_6/B_6O_6 (AA)	1.93 (I)	7.47	0	3.73	−0.32	1.62	1.36	5.85	1.61	1.36	5.87
	C_6N_6/B_6O_6 (AC)	1.76 (I)	7.38	0.55	3.36	−0.67	1.59	1.36	5.75	1.63	1.37	5.81

The atom-projected band structures (APBS) and partial density of states (PDOS) for the considered MLs, computed using PBE-GGA, are illustrated in Figs. S1(c) and S1(d) [85]. It can be seen that the C_6N_6 ML is a direct band gap semiconductor, with the conduction band minimum (CBM) and valence band maximum (VBM) located at the K point. The CBM and VBM are mainly dominated by the N atoms. On the other hand, for B_6O_6, as shown in Fig. S1(d), the CBM is mainly originated from the B atoms, while for the VBM, both B and O atoms contribute almost equally. The B_6O_6 ML is an indirect Δ semiconductor, with the CBM and VBM located at the M point and the Γ point, respectively. The calculated Δ(GGA) values for C_6N_6 and B_6O_6 MLs are 1.68 and 3.79 eV, respectively (see Table I). To achieve a more accurate depiction of the electronic properties, we additionally determined the Δ using the hybrid functional (HSE06). The HSE06-calculated Δ values are higher than those obtained using the PBE-GGA (3.21 and 5.28 eV for C_6N_6 and B_6O_6 MLs, respectively). These results exhibit a notable correspondence with prior findings [52,53,67,86]. Moreover, to account for electron-electron interactions, the QP G_0W_0 approach is employed. The resulting calculated Δ values are 4.61 and 6.12 eV for C_6N_6 and B_6O_6 MLs, respectively (as shown in Table II). Comparing the VBM and CBM energies between the GGA/PBE and G_0W_0 calculations reveals that

the influence of electron-electron interactions during the QP approach causes a shift of the CBM towards higher energies. This shift contributes to the enlargement of the Δ in G_0W_0 calculations in contrast to conventional GGA/PBE methods. While nonlocal exchange effects have been included into the HSE06 functional, it still results in a significantly smaller Δ than the G_0W_0 method. The latter shows the significant influence of the Coulomb screening effect, a factor that is effectively addressed by the self-energy operator within the G_0W_0 framework.

A. Structural and electronic properties of the C_6N_6 and B_6O_6 BLs

We considered three different stacking structures for the C_6N_6 (B_6O_6) BLs: AA, AB, and AC. The AA configuration denotes a structure in which the top and bottom layers are aligned and stacked vertically, resulting in a precise matching in the xy plane [see Figs. S2(a) and S3(a) [85]]. In the AB configuration, the top layer is shifted by approximately 1.32 Å along the x axis and 0.78 Å along the y axis (as shown in Figs. S2(b) and S3(b) [85]). In the AC-stacking, the top layer of the AA-stacking is moved 3.96 Å along the x axis and 2.27 Å along the y axis. In this configuration, the upper pore is covered by the C–N (B–O) ring of the bottom layer [Figs. 1(a) and 1(b)]. The interlayer distance (h) for the three stacking structures of C_6N_6 (B_6O_6) BLs are optimized and calculated to be 3.79 (3.86), 3.59 (3.39), and 3.33 (3.19) Å for AA-, AB-, and AC-stacking, respectively. The computed h values for AA- and AB-stacking B_6O_6 BLs are slightly larger than those reported in Ref. [53]. Notably, the h values obtained for AC-stacking C_6N_6 and B_6O_6 BLs are comparable to graphene BL determined using the PBE-D3 level (3.33 Å) [53]. The lengths of the in-plane covalent bonds remain largely unchanged across different stacking configurations. All considered BL structures maintain planarity, indicating the weak van der Waals interactions between the two layers. To evaluate the energetic stability of the stacking structures, we calculate the interface adhesion energy (E_a) using $E_a = E_{Total} - E_{TL} - E_{BL}$, where E_{Total} is the total energy of the whole stacking structure and E_{TL} (E_{BL}) is the

TABLE II. Electronic band gaps calculated by GGA, HSE06, and G_0W_0 of C_6N_6/B_6O_6 monolayers (ML), AC-stacking bilayers (BL), and AC-stacking heterostructure (HTS). For the purpose of comparing band gaps obtained from various methods, we have included GGA band gap values once again. All energy values are in eV.

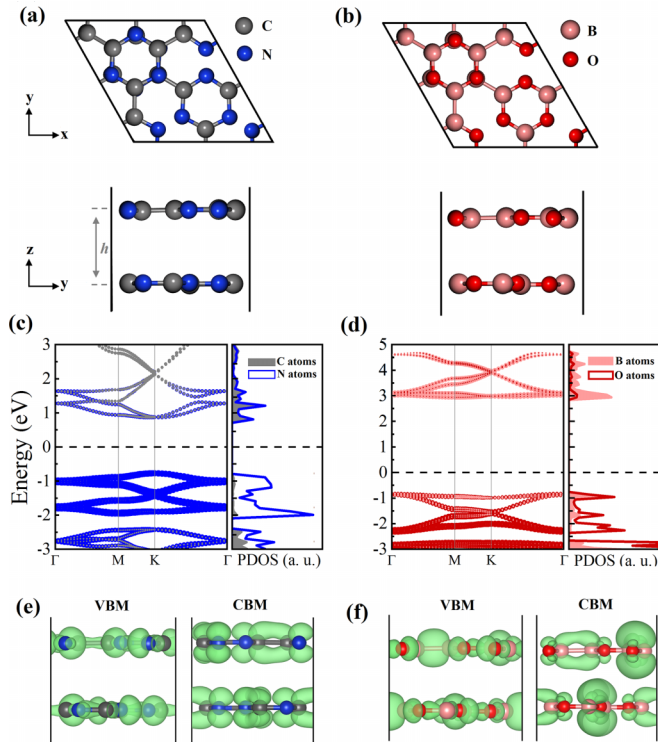|	Structure	Δ(GGA)	Δ(HSE06)	Δ(G_0W_0)
ML	C_6N_6	1.68	3.21	4.61
	B_6O_6	3.79	5.28	6.12
BL	C_6N_6 (AC)	1.45	3.16	4.36
	B_6O_6 (AC)	3.42	5.22	5.97
HTS	C_6N_6/B_6O_6 (AC)	1.76	3.07	4.64

FIG. 1. Top and side views (a), (b) and the projected band structure and partial density of states (c, d) of AC-stacking C_6N_6 and B_6O_6 BLs, calculated by PBE-GGA. Panels (e) and (f) show isosurface plots of the wave functions for the valence band maximum (VBM) and conduction band minimum (CBM) for C_6N_6 and B_6O_6.

total energy of the top (bottom) layer. Table I shows the computed values of E_a. Negative E_a in all considered layered structures imply that stacking has stabilized the system. The AC-stacking is found to be the most energetically favorable for C_6N_6 and B_6O_6 BLs, having the lowest E_a and smallest h. These findings are in agreement with the results reported for other BL systems, such as C_2N-h2D [87]. In the AC-stacking, the upper pore of the C_6N_6 (B_6O_6) ring is covered by the C–N (B–O) ring of the bottom layer, creating a repulsion between the charge centers. This repulsion is balanced by the weak vdW interaction, leading to the most stable configuration. This is similar to the case of graphite, where the repulsion between the carbon charge centers is balanced by the vdW interaction, leading to the stability of the stacked structure. Figures 1(c) and 1(d) display the PBE-GGA APBS and PDOS of C_6N_6 and B_6O_6 AC-stacking BLs, respectively. In addition, panels (c) and (d) of Figs. S2 and S3 [85] show the PBE-GGA APBS, and PDOS of the C_6N_6 and B_6O_6 BLs with AA- and AB-stacking, respectively. It is evident that the atomic distributions in the conduction band (CB) and valence band (VB) resemble those of the MLs. Our PBE-GGA calculations demonstrate that all three BL stacking configurations of C_6N_6 and B_6O_6 exhibit smaller Δ values compared to MLs, with the AA configuration having the smallest Δ (as presented in Table I). The AC-stacking BL system, with the smallest interlayer distance, has the most significant interlayer coupling. The reduced Δ of BLs compared to MLs can be attributed to the interlayer coupling-induced separation of the CB and

VB, which arises due to orbital interactions between the two layers. In the ML, the VBM is composed of σ states spread in the plane, and thus orbital hybridization and VB splitting are weak. However, in the BL system, CBM is a π-conjugated state that extends beyond the plane, leading to stronger orbital hybridization between the two layers and a greater splitting of CB. Interlayer orbital hybridization relies on precise spatial alignment of CB between the two layers. Therefore, the BL stacking order significantly affects the interaction strengths, band structures, and Δ values. This finding is in agreement with previous studies on other 2D materials, such as graphene [88] and MoS_2 [89], where Δ is also found to be strongly dependent on the stacking order.

Both AA- and AB-stacking C_6N_6 BLs have a direct Δ at the K point. However, the AC-stacking configuration shows little variation in the VBM and CBM energies between the K point and the M-K region, resulting in a slightly indirect Δ These findings are consistent with the results reported in Ref. [90], which also found a direct Δ of 1.58 eV for the AC-stacking C_6N_6 BL. The Δ behavior and the CBM and VBM positions in stacked BLs are influenced by the interlayer coupling and stacking order. The AA- and AC-stacking B_6O_6 BLs demonstrate indirect Δ, whereas the AB structure exhibits a direct Δ with both the CBM and VBM located at the Γ point. Additionally, we have computed Δ(HSE06) and Δ(G_0W_0) values for AC-stacking BLs. It is evident from Table II that these values exceed the Δ(GGA). However, the trend of Δ reduction from ML to BL is preserved in these two methods.

To gain more insights, we also plotted isosurfaces of the VBM and CBM wave functions [see Figs 1 and panels (e) and (f) of Figs. S2 and S3 [85]]. It can be seen that the VBM and CBM of C_6N_6 BLs were slightly changed. While the VBMs of B_6O_6 BLs only marginally change, the CBMs of AA- and AB-stacking are considerably moved lower, suggesting greater interlayer interactions in these structures.

B. Structural and electronic properties of the C_6N_6/B_6O_6 HTS

To study the properties of C_6N_6/B_6O_6 HTS, the unit cells of C_6N_6 and B_6O_6 are stacked on top of each other. The lattice mismatch (λ) is calculated by $\lambda = \frac{|a_{TL} - a_{BL}|}{a_{BL}} \times 100\%$, where a_{TL} and a_{BL} are the lattice constants of the top layer (C_6N_6) and the bottom layer (B_6O_6), respectively. The computed value of λ is 9.07%, indicating a moderate lattice mismatch between the two materials.

The stacked HTS is optimized using the same computational methodology as for the individual MLs and BLs, with the atomic positions and cell parameters allowed to relax until the total energy converges. Two possible stacking orders for C_6N_6/B_6O_6 HTS (AA- and AC-stacking) are shown in Fig. 2(a) and 2(b). The stacking configurations are similar to the aforementioned bilayer structures. The AB-stacking system was deformed, rendering it unstable. In the AA structure, the two hexagonal lattices perfectly overlap each other within the optimized lattice constant of 7.46 Å, and the C (N) atoms are located on top of the B (O) atoms. Upon full optimization, this structure maintains its planarity, with an interlayer distance of about 3.73 Å, which is comparable to the AA-stacking C_6N_6 bilayer.
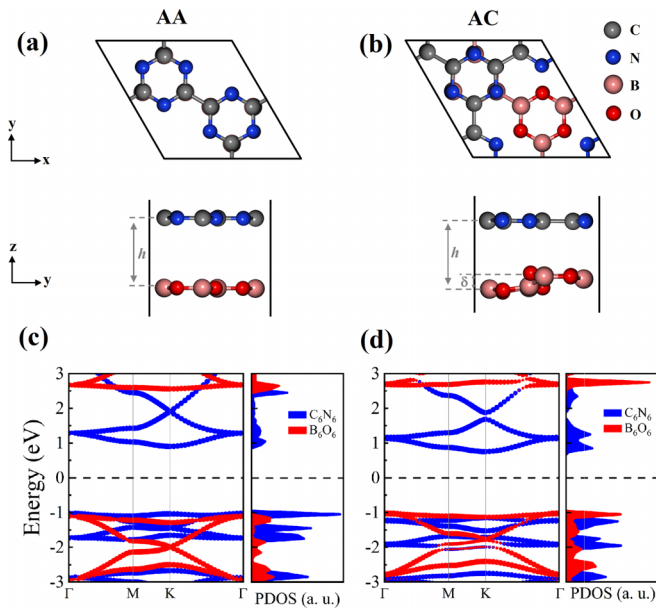
FIG. 2. Top and side views of (a) AA and (b) AC-stacking configurations of the C_6N_6/B_6O_6 HTS. The PBE-GGA calculated projected band structure (left-hand panel) and partial density of states (right-hand panel) of the (c) AA-stacking and (d) AC-stacking configurations of the C_6N_6/B_6O_6 HTS. The interlayer distance and buckling of layers are illustrated by h and δ. Blue and red lines represent the contribution of C_6N_6 and B_6O_6, respectively. The Fermi energy is set to zero.

In the AC-stacking HTS, the C_6N_6 monolayer is shifted by approximately 3.69 Å along the x axis and 2.10 Å along the y axis, and the top pore of the C_6N_6 layer covered by the hexagonal B–O ring of the bottom layer. Compared to the AA-stacking HTS, the AC-stacking exhibits significant surface buckling of around 0.55 Å, indicating a stronger interface interaction between the layers. Similar layer distortions have been found in some stacking arrangements of the C_6N_6/C_3N_4 HTS and h-BN BLs with monovacancy, indicating a stronger interaction between the layers [69,91]. The optimal h for the AC-stacking HTS is 3.36 Å, which is almost 10% smaller than that of the AA-stacking HTS. The adhesion energy calculations indicate that the AC arrangement is more energetically favorable than the AA configuration. Taking these into consideration, the AC-stacking system suggests greater thermodynamic stability and stronger interaction between MLs due to the lower E_a, shorter h, and surface wrinkling of B_6O_6. The structural parameters for both HTS are summarized in Table I.

In order to verify the thermal stability of the AA- and AC-stacking C_6N_6/B_6O_6 HTS, we performed *ab initio* molecular dynamics (AIMD) simulations at room temperature using the NVT ensemble (see Movies S1–S4 in the Supplemental Material [85]). The AIMD simulations showed that both AA- and AC-stacking HTS remain stable throughout the simulation period, and their structural properties remain nearly constant. Furthermore, the average h for the AA- and AC-stacking HTS remain at approximately 3.73 and 3.36 Å, respectively, indicating that the structures maintain their initial configuration.

Figures 2(c) and 2(d) show the electronic band structures and PDOS plots of the AA- and AC-stacking HTS, obtained by PBE-GGA. The contribution of the C_6N_6 and B_6O_6 layers are displayed using blue and red colors, respectively. Both the AA- and AC-stacking HTS maintain their semiconducting nature, with indirect Δ(GGA) of 1.93 and 1.76 eV, respectively, with the VBM at the Γ point and the CBM at the K point. It is also evident from Fig. 2(c) that the intrinsic electronic properties of the isolated MLs are still preserved due to the large equilibrium h for the C_6N_6/B_6O_6 AA HTS (3.73 Å) and weak vdW interaction between layers. Despite being a type I HTS where the VBM and CBM are both occupied by the C_6N_6 layer, the calculated Δ(1.93 eV) is larger than that of the monolayer C_6N_6 (1.68 eV). This suggests that the weak interaction with the B_6O_6 layer has influenced the band structure, leading to an increase in Δ Additionally, PDOS in Fig. 2(c) shows that both VB and CB are mostly contributed by C_6N_6 layer.

For the AC-stacking system, the PBE-GGA band structure and PDOS indicate that the VBM primarily originates from the B_6O_6 layer, while the CBM is mainly distributed by the C_6N_6 layer [Fig. 2(d)], resulting in a type II HTS. It is also clearly confirmed by the VBM and CBM wave functions of AA and AC HTS, shown in Fig. 3(a). The wave function distributions of the VBM and CBM for the AA- and AC-stacking HTS provide important information on the type of band alignment present in the C_6N_6/B_6O_6 HTS. In a type I band alignment, both the VBM and CBM are located in the same layer. However, in a type II band alignment, the VBM and CBM are located in different layers. Figure 3(b) schematically shows the VBM and CBM alignments of layers for the two considered HTS. The VBM offset (ΔE_V) and CBM offset (ΔE_C) values between the C_6N_6 and B_6O_6 layers are 0.02 eV and 1.67 eV for the AA HTS, and 0.05 eV and 1.93 eV for the AC HTS. In the AC configuration of the C_6N_6/B_6O_6 HTS, the CB and VB levels of C_6N_6 are found to have higher potentials than the corresponding levels of B_6O_6. This suggests that photogenerated electrons in B_6O_6 tend to migrate to the CB of C_6N_6.

For precise determination of the band edge positions, we compute the vacuum level by averaging the constant potential region within the electrostatic potential obtained from the HSE06 functional [see Figs. 4(a) and 4(b)]. The work functions (Φ) of the AA- and AC-staking HST, which is commonly used as an intrinsic reference for band alignment, are also shown. As can be seen, Φ is found to be 5.38 and 5.4 eV for the AA and AC configurations, respectively. A lower value of Φ means that electron transitions would be facilitated between VBM and CBM edges under light irradiation [92].

The calculated macroscopic average potential [$\Delta V(z)$] for AA and AC HTS is found to be 1.79 and 9.68 eV, respectively. The large $\Delta V(z)$ for the AC configuration can lower the photoexcited electron-hole recombination rate and thus enhance the power conversion efficiency [93]. Figure 4(c) shows the VBM and CBM positions shifted by the local vacuum level to zero energy which allows us to explore the thermodynamic feasibility of the photocatalytic processes. As depicted, the VBM positions of the B_6O_6 and C_6N_6 MLs and their HTS are below the redox potentials of the oxygen evolution reaction (O_2/H_2O) at pH = 0 (-5.67 eV), and the
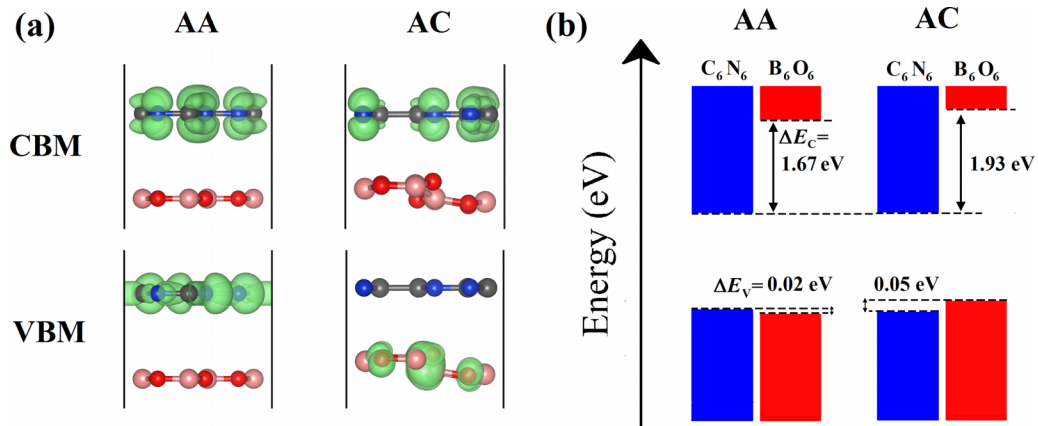
FIG. 3. (a) Isosurface plots of the VBM and CBM wave functions for C_6N_6/B_6O_6 HTS. (b) Schematic presentation of the conduction and valence band alignments for AA- and AC-stacking of C_6N_6/B_6O_6 HTS, calculated by PBE-GGA. The VBM offset (ΔE_V) and CBM offset (ΔE_C) between the C_6N_6 and B_6O_6 layers are also shown.

CBM positions of the MLs and HTS are above the reduction potential of H^+/H_2 at pH = 0 (-4.44 eV). The latter and the fact that their Δ are larger than 1.23 eV (difference between the hydrogen and oxygen evolution reaction levels) indicate that they can facilitate the overall water splitting reactions.
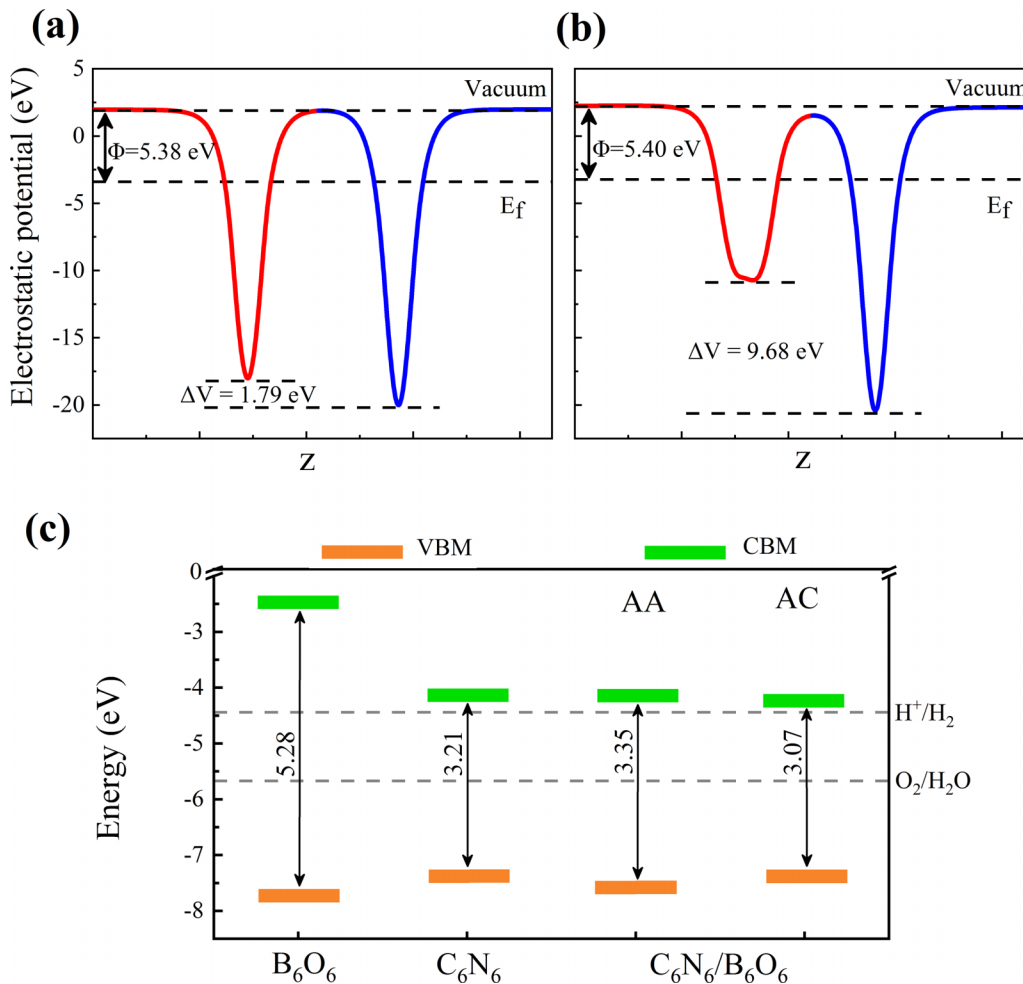

FIG. 4. Electrostatic potential of the AA-stacking (a) and AC-stacking (b) C_6N_6/B_6O_6 heterostructures. (c) The band alignment of the B_6O_6 and C_6N_6 monolayers and the two considered heterostructures, referring to the vacuum level. This alignment is determined using the HSE06 functional. Dashed lines indicate the energy levels corresponding to redox potentials of water splitting at pH = 0.
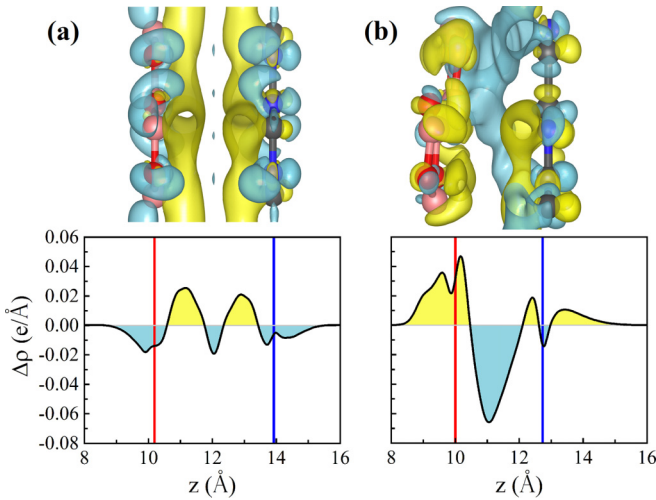
FIG. 5. The plane-averaged charge density difference $[\Delta\rho(z)]$ along the normal direction of the heterostructure. The three-dimensional (3D) isosurface of charge density difference is displayed above the diagram. The yellow and blue areas represent electrons accumulation and depletion, respectively. The vertical red and blue lines denote C_6N_6 and B_6O_6 layers, respectively.

FIG. 6. G_0W_0-BSE optical absorption spectra of C_6N_6, B_6O_6, AC-stacking bilayer C_6N_6, AC-stacking bilayer B_6O_6, and AC-stacking C_6N_6/B_6O_6 heterostructure, along with the averaged direction, represented by blue, red, dashed blue, dashed red, and purple lines, respectively.

The calculated Δ(HSE06) for the AA and AC configurations are 3.35 and 3.07 eV, respectively. Notably, the Δ(HSE06) for the AC configuration has shown a reduction compared to the C_6N_6 ML, which is contrary to the Δ(GGA) trend. The $\Delta(G_0W_0)$ for the AC-stacking configuration (4.64 eV as presented in Table II) follows a pattern similar to PBE-GGA, increasing from the C_6N_6 ML.

Furthermore, to investigate the charge transfer at the interface of the C_6N_6/B_6O_6 HTS, we analyzed the charge density difference by $\Delta\rho = \rho_{Total} - \rho_{TL} - \rho_{BL}$, where ρ_{Total}, ρ_{TL}, and ρ_{BL} represent the charge density of the C_6N_6/B_6O_6 HTS, the top layer (C_6N_6), and the bottom layer (B_6O_6), respectively. The 3D isosurface of the charge density difference and the planar-averaged charge density difference along the z direction are presented on the top and bottom sides of Fig. 5. The positive (yellow area) and negative (blue area) values in the 3D isosurface of charge density difference indicate the accumulation and depletion of charge, respectively. The weak vdW interactions between the layers are clearly seen by the charge redistribution in the interfacial region. As shown in Fig. 5(a), the AA HTS exhibits only a small charge redistribution, while there is a significant charge transfer from the B_6O_6 layer toward the C_6N_6 layer in the AC HTS, resulting in a built-in electric field directed from the B_6O_6 to the C_6N_6. The charge transfer mechanism at the C_6N_6/B_6O_6 interface can be directly understood from the band alignment shown in Fig. 3(b), where electrons are transferred from the CBM of B_6O_6 to that of C_6N_6, while holes are transferred from the VBM of C_6N_6 to that of B_6O_6. Moreover, based on the Bader charge analysis of the AC HTS, it was found that the net charges of B_6O_6 and C_6N_6 are roughly 0.005 e and -0.005 e, respectively. In other words, the charge is transferred from the B_6O_6 layer to the C_6N_6 layer, which is in agreement with the charge density difference shown in Fig. 5(b).
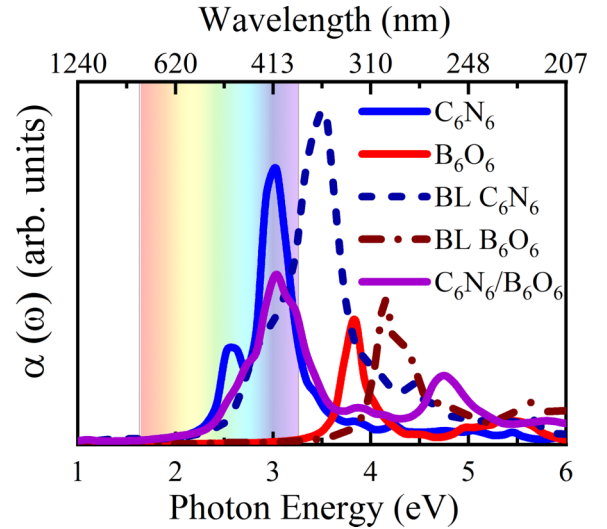
C. Optical properties of AC-stacking C_6N_6/B_6O_6 HTS

Type II HTS offer a promising platform for optoelectronic applications due to their unique optical properties. The spatial separation of electron and hole wave functions in type II HTS reduces the probability of recombination, resulting in the creation of longer-lived excitons compared to type I HTS. These properties make type II HTS highly desirable for applications such as photovoltaic cells and light-emitting diodes. Therefore, investigating the optical properties of the C_6N_6/B_6O_6 type II HTS is of great importance in understanding its potential for practical applications. In addition, the type II band alignment of the C_6N_6/B_6O_6 HTS provides a built-in electric field that can further enhance the separation of electron-hole pairs. This built-in electric field can be utilized for efficient charge separation and collection in photovoltaic devices, leading to higher power conversion efficiency. The optical properties are calculated using the G_0W_0-BSE method, which incorporates excitonic effects. Theoretical absorption spectra directly correlate with the imaginary part of the dielectric function $[\text{Im}\epsilon(\omega)]$. The optical absorption spectra $[\alpha(\omega)]$ of the AC-stacking B_6O_6/C_6N_6 HTS is shown in Fig. 6, highlighting the visible light energy range of 1.63–3.26 eV. Additionally, for comparison, $\alpha(\omega)$ of the MLs and AC-stacking BLs are also included. The first excitonic peak in $\alpha(\omega)$ corresponds to the optical gap (Δ_o) [94]. As can be seen from Fig. 6, the obtained Δ_o for C_6N_6 and B_6O_6 MLs are 2.58 and 3.83 eV, respectively. The exciton binding energy (E_b), representing the energy difference between the $\Delta(G_0W_0)$ and the BSE Δ_o, is calculated to be 2.03 eV for C_6N_6 ML and 2.27 eV for B_6O_6 ML. The high E_b can be attributed to electron-hole excitations, which play a crucial role in optical absorption at energies lower than $\Delta(G_0W_0)$. Such large E_b values have been reported in other 2D materials such as chlorographene, fluorographene, graphane, nitrogen phosphide, and hexagonal boron nitride [95–97]. Moreover,

TABLE III. Structural parameters of AC-stacking C_6N_6/B_6O_6 heterostructure under in-plane biaxial strain (ϵ), including the bond length between C–C atoms (d_{C-C}), bond length between C–N atoms (d_{C-N}), bond length between B–B atoms (d_{B-B}), bond length between B–O atoms (d_{B-O}), interlayer distance between two layers (h), buckling of B_6O_6 layer (δ), (all bond lengths are given in Å), calculated electronic band gap [Δ(eV)], and strain energy [E_s (eV)].

| ϵ (%)	d_{C-C}	d_{C-N}	d_{B-B}	d_{B-O}	δ	h	Δ	E_s
−4	1.49	1.34	1.65	1.37	0.85	3.61	1.62	0.60
−3	1.51	1.35	1.65	1.37	0.78	3.55	1.64	0.32
−2	1.54	1.35	1.64	1.37	0.69	3.43	1.67	0.13
−1	1.56	1.36	1.64	1.37	0.61	3.39	1.73	0.02
0	1.59	1.36	1.63	1.37	0.55	3.36	1.76	0.00
1	1.62	1.36	1.64	1.37	0.40	3.31	1.87	0.04
2	1.65	1.37	1.64	1.37	0.26	3.26	1.95	0.15
3	1.69	1.37	1.65	1.37	0.15	3.22	2.02	0.35
4	1.73	1.37	1.67	1.37	0.09	3.21	2.08	0.63

FIG. 7. Valence band maximum (VBM) and the conduction band minimum (CBM) of the AC-stacking heterostructure with regard to different compressive (a) and tensile (b) strains. The Fermi level is set to zero.

$\Delta_o = 3$ eV of the HTS is redshifted compared to that of B_6O_6, which can be attributed to the formation of a type II band alignment, the rearrangement of charges and the coupling of interfacial layers. The absorption spectra analysis reveals that the B_6O_6 ML mainly responds to ultraviolet light with a wavelength shorter than 400 nm, while both the C_6N_6 ML and the AC HTS exhibit visible-light responses in the range of 400–600 nm. Therefore, constructing the C_6N_6/B_6O_6 HTS can significantly improve the light absorption strength and extend the light reaction range. In compared to the MLs, the $\alpha(\omega)$ of the BL structures demonstrates a blueshift with a slight increase. The calculated Δ_o values for C_6N_6 and B_6O_6 BLs are 3.48 and 4.15 eV, respectively. The latter is attributed to the formation of interlayer excitons resulting from the coupling of electronic excitations in the two layers. The calculated E_b values for the AC configurations of C_6N_6 BL, B_6O_6 BL, and C_6N_6/B_6O_6 HTS are 0.88, 1.82, and 1.62, respectively, representing a decrease compared to those obtained for MLs. This is due to the significant interplay between Coulomb interactions and excitonic effects in optical properties and aligns with the findings for C_2N, where excitonic effects weaken as the number of layers increases [98].

D. Effects of strain on the optoelectronic properties of AC-stacking C_6N_6/B_6O_6 HTS

The electronic properties of materials, including the band gap, can be significantly influenced by applying strain. The effects of in-plane biaxial strain on Δ for the AC-stacking C_6N_6/B_6O_6 HTS are investigated in this section. We achieve this by symmetrically expanding or reducing the hexagonal unit cell with particular ratios, $\epsilon = (a \pm a_0)/a_0$, where a and a_0 are the lattice constants of the strained and unstrained structure. Based on the optimized atomic arrangement, we have determined that an in-plane biaxial strain range of −4% to 4% (with an interval of 1%) is suitable for our analysis. The structural parameters and corresponding Δ values for the studied in-plane biaxial strains are presented in Table III. As can be seen, the length of the C–C bond considerably increases (decreases) with the increase of tensile (compressive) biaxial
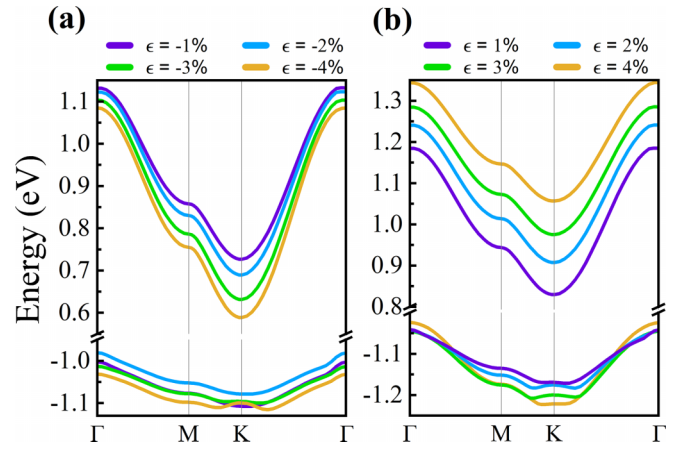
strain. The bond length between C and N atoms also shows a slight variation following the same trend. This finding is consistent with the results obtained for C_6N_6 ML under tensile strain [49]. On the other hand, the B–B bond length slowly stretches with increasing tensile and compressive strains, while d_{B-O} remains constant. This can be attributed to the shorter bond length and greater interatomic contact and covalent bonding between the B and O atoms. Notably, the response of the B_6O_6 layer to the applied strains is primarily in changing the buckling of the B_6O_6 layer (δ). Our calculations show that h reduces linearly as the tensile strain increases, while it enhances with increasing compressive strain. This behavior can be explained by the change in the bond length between the layers under strain. A strong correlation was found between h and Δ, with a negative correlation coefficient of −0.93. As h decreases with increasing tensile strain, Δ increases, resulting in a larger separation between the VB and CB. The same trend for strain-tunable Δ has also been found in hydrogenated BL graphene [99]. Having only small Δ variations in C_6N_6 and B_6O_6 MLs compared to the HTS, highlights the significance of h in determining Δ modification [49,52]. Additionally, a high positive correlation was found between δ and both h and Δ, with correlation coefficients of 0.96 and −0.99, respectively. As δ increases, h also increases, leading to a decrease in Δ. This indicates that the electronic properties of the C_6N_6/B_6O_6 HTS can be significantly influenced by changing h.

Figures 7(a) and 7(b) demonstrate remarkable changes in the electronic properties of AC-stacking C_6N_6/B_6O_6 HTS under both compressive and tensile biaxial strains. Notably, tensile strains induce a more significant shift in Δ than compressive strains. Under compressive and tensile strains, Δ undergoes substantial changes, with minimum and maximum values of 3.21 and 3.61 eV found at −4% and 4% strains, respectively. Specifically, under compressive strain, the energy of the CBM at the K point decreases, while the energy of the VBM at the Γ point first increases (when the induced strain equals −2%) and then decreases. Conversely, under increasing tensile strain, the energy of the CBM at the K point

increases, while the energy of the VBM at the Γ point remains nearly constant.

We also investigated the effect of biaxial strain on C_6N_6 and B_6O_6 MLs to acquire a more comprehensive insight into the changes in band structure caused by strain. As shown in Fig. S5(a) [85], it is evident that under compressive biaxial strains, Δ of the C_6N_6 ML retains its direct characteristic, with both the VBM and CBM positioned at the K point. Δ decreases as compressive strain increases (see Fig. S5 [85]). Within the tensile strain range of 2% to 4%, the VBM changes to the Γ point, while the CBM remains at the K point, resulting in an indirect Δ.

Applying compressive strain to B_6O_6 ML results in a slight rightward shift of the CBM from the K point. The VBM is still located at the Γ point, and Δ remains indirect. As compressive strain increases, Δ decreases from 3.79 to 3.26 eV. On the other hand, under tensile strains of 3% and 4%, the CBM shifts to the Γ point, resulting in a direct Δ. Applying tensile strain decrease Δ almost linearly to 3.49 eV. As depicted in Fig. S6 [85], the highest Δ value for the B_6O_6 ML is obtained in the unstrained state. Comparing the strain-induced changes in Δ between MLs and HTS shows that the Δ changes in HTS are slower than the MLs. Furthermore, considering that the CBM of HTS originates from the C_6N_6 [as previously illustrated in Fig. 2(d)], its strain-induced changes closely resemble those of C_6N_6. The strain energy has also been calculated in order to evaluate the stability of the strained systems and confirm that the stresses considered do not exceed the elastic limit. This parameter is defined as the difference between the total energy of the strained (E_ϵ) and unstrained (E_0) structures, i.e., $E_s = E_\epsilon - E_0$. From Table II, E_s increases quadratically, indicating that the strains are within the elastic deformation limit. This means that the applied stresses are not causing permanent deformation in the material. Therefore, the system is structurally stable under the applied strains. It is noteworthy that the unstrained structure has the lowest value of E_s, indicating that it is the most stable configuration.

The relation between the strain energy per area (E_s/A) and the strain is shown in Fig. S4 [85]. This figure clearly illustrates the nonlinear effect, as the value of E_s/A at -4% strain is approximately 12% greater than the value at 4% strain. By polynomial fitting of this curve, the Young's modulus is calculated to be $Y = 132.24$ N/m, which is slightly lower than the Young's modulus of C_6N_6 (133.55 N/m [100]) and higher than the Young's modulus of B_6O_6 (71.83 N/m [52]).

Additionally, we investigated the influence of applied biaxial strain on Δ_o. Due to computational constraints, we limited our G_0W_0-BSE calculations of Δ_o to strains of -4% and 4%. The calculated Δ_o for HTS under strain are found to be 2.92 eV for -4% strain and 3.32 eV for 4% strain. The latter can be attributed to changes in the band structure of AC-stacking C_6N_6/B_6O_6 HTS under tensile and compressive strain. The application of tensile strain widens Δ, resulting in an increase in Δ_o. Tensile strain increases the separation between the CB and VB, reducing the probability of electron transition and increasing the energy required for it to occur. This results in a widening of Δ and a subsequent increase in Δ_o. Conversely, compressive strain brings the VB and CB closer together, causing a reduction in Δ and a corresponding decrease in Δ_o. Therefore, the optical absorption spectra of
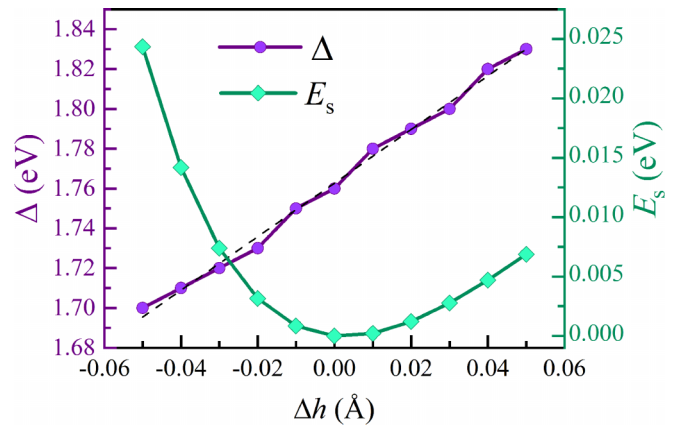

FIG. 8. Out-of-plane strain effects on the electronic band gap (Δ) and strain energy (E_s). The black dashed line indicates linear fit ($\Delta = 1.34\Delta h + 1.76$).

AC-stacking C_6N_6/B_6O_6 HTS can also be affected by the application of strain. These values indicate slight red and blue shifts, respectively, as compared to the unstrained HTS configuration. These shifts can be attributed to variations in the interlayer distance. As the interlayer distance increases, the optical gap decreases, aligning with the findings of Ref. [101].

In addition to in-plane strain, out-of-plane vertical strains may cause Δ to change. The effect of out-of-plane vertical strain on the band structure is investigated by varying the vertical distance between the two MLs. Figure 8 shows the variation of Δ and E_s as a function of the interlayer distance difference, $\Delta h = h'-h$, where h' and h are the modified and initial interlayer distances, respectively. The studied range of Δh is from -0.5 to 0.5 Å (with a span of 0.1 Å). As shown in Fig. 8, E_s calculations indicate that the unstrained system, where the interlayer distance is 3.36 Å, is the most stable state. Furthermore, Δ decreases (increases) linearly with decreasing (increasing) of h. It should be noted that this linear relationship has a slope of 1.34 (the fitted line shown by a black dashed line in the plot), indicating a strong correlation between Δ and h. The changes of Δ under decreasing h are
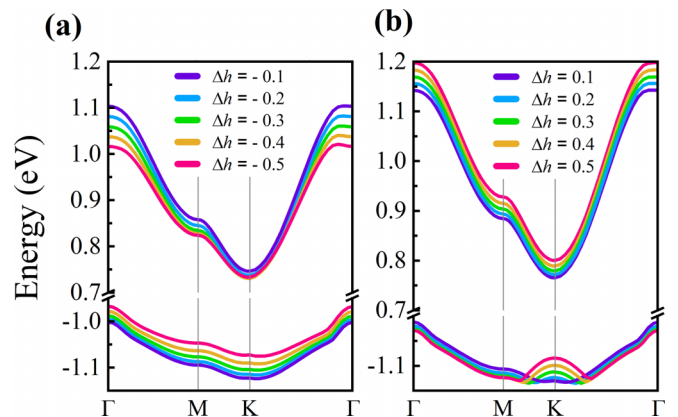

FIG. 9. The valence band maximum (VBM) and the conduction band minimum (CBM) of the AC-stacking heterostructure with regard to different compressed (a) and extended (b) interlayer distances. The Fermi level is set to zero.

mainly due to the slight up-shift in the VBM. In contrast, with the increased h, the CBM at the K point moves upward while the changes in VBM are negligible (see Fig. 9).

IV. CONCLUSION

In conclusion, our density functional theory calculations, incorporating van der Waals corrections and considering excitonic effects within the G_0W_0-BSE approach, have provided significant insights into the electronic and optical properties of various stacking configurations of C_6N_6 and B_6O_6 bilayers and heterostructures. Our findings indicate that the energetically favorable configuration is the AC-stacking, where the hexagonal ring of the lower layer covers the pore in the upper layer. The AC-stacking bilayers have a planar structure, while the AC-stacking heterostructures exhibit a notable surface buckling of approximately 0.55 Å, indicating a stronger interface interaction. We have also determined that the indirect band gap of the type II AC heterostructure is 1.76 eV, and the band edge alignments for C_6N_6 and B_6O_6 monolayers and heterostructures are suitable for the photocatalytic splitting of water. Moreover, we found that the AC heterostructure exhibits a redshift in optical absorption and has visible-light responses, which can improve its solar energy conversion efficiency. Additionally, we have demonstrated the effects of in-plane and out-of-plane strains on the modification of the band gap of the AC heterostructure. Under compressive and tensile biaxial strains, the band gap undergoes significant changes, with minimum and maximum values of 1.62 and 2.08 eV found at -4% and 4% strains, respectively. We have also observed strong negative correlations, with correlation coefficients of -0.93 and -0.99, respectively, between the interlayer distance and band gap and between the buckling height and band gap. Overall, our study provides a solid theoretical foundation for future experimental investigations and suggests potential applications in optoelectronic devices.

ACKNOWLEDGMENT

[1] X. Zou, H. Ren, and G. Zhu, Chem. Commun. **49**, 3925 (2013).

[2] S. Zhang, Q. Yang, C. Wang, X. Luo, J. Kim, Z. Wang, and Y. Yamauchi, Adv. Sci. **5**, 1801116 (2018).

[3] J.-X. Jiang and A. I. Cooper, Top. Curr. Chem. **293**, 1 (2010).

[4] J. Hou, H. Zhang, G. P. Simon, and H. Wang, Adv. Mater. **32**, 1902009 (2020).

[5] H. Chan Wai, M. Mohd Noor, Z. A. Ahmad, S. B. Jamaludin, M. A. Mohd Ishak, and M. S. Jusoh, Adv. Mater. Res. **795**, 96 (2013).

[6] A. H. Dabwan, I. Daizo, S. Kaneco, I. Senmatsu, K. Nakahama, H. Katsumata, T. Suzuki, and O. Kiyohisa, J. Environ. Sci. **20**, 172 (2008).

[7] K. Ishizaki, S. Komarneni, and M. Nanko, *Porous Materials Process Technology and Applications* (Kluwer Academic Publishers, Dordrecht, The Netherlands, 1998), p. 202.

[8] Q. Sun, B. Aguila, Y. Song, and S. Ma, Acc. Chem. Res. **53**, 812 (2020).

[9] M.-H. Sun, S.-Z. Huang, L.-H. Chen, Y. Li, X.-Y. Yang, Z.-Y. Yuan, and B.-L. Su, Chem. Soc. Rev. **45**, 3479 (2016).

[10] Z. Wu and C. Y. Zhao, Solar Energy **85**, 1371 (2011).

[11] C. Perego and R. Millini, Chem. Soc. Rev. **42**, 3956 (2013).

[12] N. Singh, S. Son, J. An, I. Kim, M. Choi, N. Kong, W. Tao, and J. S. Kim, Chem. Soc. Rev. **50**, 12883 (2021).

[13] M.-X. Wu and Y.-W. Yang, Chinese Chem. Lett. **28**, 1135 (2017).

[14] A. I. Cooper, Adv. Mater. **21**, 1291 (2009).

[15] J.-S. M. Lee and A. I. Cooper, Chem. Rev. **120**, 2171 (2020).

[16] T. Ben and S. Qiu, Cryst. Eng. Comm. **15**, 17 (2013).

[17] Y. Tian and G. Zhu, Chem. Rev. **120**, 8934 (2020).

[18] N. B. McKeown, ISRN Mater. Sci. **2012**, 513986 (2012).

[19] N. B. McKeown, Sci. China Chem. **60**, 1023 (2017).

[20] X. Feng, X. Ding, and D. Jiang, Chem. Soc. Rev. **41**, 6010 (2012).

[21] S.-Y. Ding and W. Wang, Chem. Soc. Rev. **42**, 548 (2013).

[22] P. J. Waller, F. Gándara, and O. M. Yaghi, Acc. Chem. Res. **48**, 3053 (2015).

[23] L. J. Abbott and C. M. Colina, Macromolecules **47**, 5409 (2014).

[24] C. S. Diercks and O. M. Yaghi, Science **355**, eaal1585 (2017).

[25] D.-G. Wang, T. Qiu, W. Guo, Z. Liang, H. Tabassum, D. Xia, and R. Zou, Energy Environ. Sci. **14**, 688 (2021).

[26] H. R. Abuzeid, A. F. EL-Mahdy, and S.-W. Kuo, Giant **6**, 100054 (2021).

[27] X. Ding, J. Guo, X. Feng, Y. Honsho, J. Guo, S. Seki, P. Maitarad, A. Saeki, S. Nagase, and D. Jiang, Angew. Chem. Int. Ed. **50**, 1289 (2011).

[28] P. Zhu and V. Meunier, J. Chem. Phys. **137**, 244703 (2012).

[29] S. Pakhira, K. P. Lucht, and J. L. Mendoza-Cortes, J. Phys. Chem. C **121**, 21160 (2017).

[30] S. Pakhira and J. L. Mendoza-Cortes, Phys. Chem. Chem. Phys. **21**, 8785 (2019).

[31] H. V. Babu, M. G. M. Bai, and M. Rajeswara Rao, ACS Appl. Mater. Interfaces **11**, 11029 (2019).

[32] F. Yu, W. Liu, S.-W. Ke, M. Kurmoo, J.-L. Zuo, and Q. Zhang, Nat. Commun. **11**, 5534 (2020).

[33] T. Feng, D. Streater, B. Sun, K. Duisenova, D. Wang, Y. Liu, J. Huang, and J. Zhang, J. Phys. Chem. Lett. **13**, 1398 (2022).

[34] S. Pakhira, M. Takayanagi, and M. Nagaoka, J. Phys. Chem. C **119**, 28789 (2015).

[35] U. Díaz and A. Corma, Coordin. Chem. Rev. **311**, 85 (2016).

[36] C. Shao, Q. He, M. Zhang, L. Jia, Y. Ji, Y. Hu, Y. Li, W. Huang, and Y. Li, Chinese J. Catalysis **46**, 28 (2023).

[37] C. Steiner, J. Gebhardt, M. Ammon, Z. Yang, A. Heidenreich, N. Hammer, A. Görling, M. Kivala, and S. Maier, Nat. Commun. **8**, 14765 (2017).

[38] A. M. Evans, L. R. Parent, N. C. Flanders, R. P. Bisbey, E. Vitaku, M. S. Kirschner, R. D. Schaller, L. X. Chen, N. C. Gianneschi, and W. R. Dichtel, Science **361**, 52 (2018).

[39] M. Tong, Y. Lan, Q. Yang, and C. Zhong, Chem. Eng. Sci. **168**, 456 (2017).

[40] S. Thomas, H. Li, C. Zhong, M. Matsumoto, W. R. Dichtel, and J.-L. Bredas, Chem. Mater. **31**, 3051 (2019).

[41] L. Liang, P. Zhu, and V. Meunier, J. Chem. Phys. **142**, 184708 (2015).

[42] A. Hashmi, M. U. Farooq, I. Khan, J. Son, and J. Hong, J. Mater. Chem. A **5**, 2821 (2017).

[43] A. Fu, G. Yi, and Y. Li, J. Phys. Chem. C **126**, 20127 (2022).

[44] S. Guan, Y. Cheng, C. Liu, J. Han, Y. Lu, S. A. Yang, and Y. Yao, Appl. Phys. Lett. **107**, 231904 (2015).

[45] C. Cao, F. Huang, C. Cao, J. Li, and H. Zhu, Chem. Mater. **16**, 5213 (2004).

[46] J. Li, C. Cao, J. Hao, H. Qiu, Y. Xu, and H. Zhu, Diam. Relat. Mater. **15**, 1593 (2006).

[47] K. Srinivasu, B. Modak, and S. K. Ghosh, J. Phys. Chem. C **118**, 26479 (2014).

[48] A. Wang, X. Zhang, and M. Zhao, Nanoscale **6**, 11157 (2014).

[49] H. Li, H. Hu, C. Bai, C. Bao, F. Guo, Z. Feng, and Y. Liu, RSC Adv. **9**, 7464 (2019).

[50] A. Bafekry, C. Stampfl, B. Akgenc, B. Mortazavi, M. Ghergherehchi, and Ch. V. Nguyen, Phys. Chem. Chem. Phys. **22**, 6418 (2020).

[51] M. Stredansky, A. Sala, T. Fontanot, R. Costantini, C. Africh, G. Comelli, L. Floreano, A. Morgante, and A. Cossaro, Chem. Commun. **54**, 3971 (2018).

[52] S. Lin, J. Gu, H. Zhang, Y. Wang, and Z. Chen, Flat. Chem. **9**, 27 (2018).

[53] S. Ullah, P. A. Denis, and F. Sato, RSC Adv. **9**, 37526 (2019).

[54] R. Rahimi and M. Solimannejad, J. Mol. Liq. **354**, 118855 (2022).

[55] N. U. Rahman, A. A. Khan, R. Ullah, R. Ahmad, and I. Ahmad, Surfaces Interfaces **29**, 101767 (2022).

[56] S. Yang, C. Wang, H. Sahin, H. Chen, Y. Li, S.-S. Li, A. Suslu, F. M. Peeters, Q. Liu, J. Li *et al.*, Nano Lett. **15**, 1660 (2015).

[57] M. Neek-Amal and F. M. Peeters, Phys. Rev. B **85**, 195446 (2012).

[58] M. Neek-Amal, J. Beheshtian, A. Sadeghi, K. Michel, and F. M. Peeters, J. Phys. Chem. C **117**, 13261 (2013).

[59] B. Amorim, A. Cortijo, F. de Juan, A. G. Grushin, F. Guinea, A. Gutiérrez-Rubio, H. Ochoa, V. Parente, R. Roldán, P. San-Jose *et al.*, Phys. Rep. **617**, 1 (2016).

[60] P. T. T. Le, N. N. Hieu, L. M. Bui, H. V. Phuc, B. D. Hoi, B. Amin, and C. V. Nguyen, Phys. Chem. Chem. Phys. **20**, 27856 (2018).

[61] A. Bafekry and M. Neek-Amal, Phys. Rev. B **101**, 085417 (2020).

[62] M. Sharma, A. Kumar, P. K. Ahluwalia, and R. Pandey, J. Appl. Phys. **116**, 063711 (2014).

[63] G. G. Naumis, Rev. Mex. Fis. **67**, 050102 (2021).

[64] A. Bafekry, M. Neek-Amal, and F. M. Peeters, Phys. Rev. B **101**, 165407 (2020).

[65] M. Neek-Amal and F. M. Peeters, Appl. Phys. Lett. **104**, 041909 (2014).

[66] J. Wang, Y. Huang, F. Ma, J. Zhang, X. Wei, G. Zhu, and P. Du, Mater. Today Commun. **26**, 101969 (2021).

[67] M. Mukherjee, R. Jana, and A. Datta, Phys. Chem. Chem. Phys. **23**, 3925 (2021).

[68] J. Chang, N. Dong, G. Wang, L. Jiang, H. Yuan, and H. Chen, Appl. Surf. Sci. **554**, 149465 (2021).

[69] D. Liang, T. Jing, Y. Ma, J. Hao, G. Sun, and M. Deng, J. Phys. Chem. C **120**, 24023 (2016).

[70] H. Wenna, C. Xuefeng, R. Minglei, P. Fengzhu, P. Chengxiao, Y. Haigang, G. Qinfen, W. Bing, and Y. Huabing, J. Phys. D **55**, 264001 (2022).

[71] P. Giannozzi, S. Baroni, N. Bonini, M. Calandra, R. Car, C. Cavazzoni, D. Ceresoli, G. L. Chiarotti, M. Cococcioni, I. Dabo *et al.*, J. Phys.: Condens. Matter **21**, 395502 (2009).

[72] P. Giannozzi, O. Andreussi, T. Brumme, O. Bunau, M. B. Nardelli, M. Calandra, R. Car, C. Cavazzoni, D. Ceresoli, M. Cococcioni *et al.*, J. Phys.: Condens. Matter **29**, 465901 (2017).

[73] M. Dion, H. Rydberg, E. Schröder, D. C. Langreth, and B. I. Lundqvist, Phys. Rev. Lett. **92**, 246401 (2004).

[74] T. Thonhauser, V. R. Cooper, S. Li, A. Puzder, P. Hyldgaard, and D. C. Langreth, Phys. Rev. B **76**, 125112 (2007).

[75] H. J. Monkhorst and J. D. Pack, Phys. Rev. B **13**, 5188 (1976).

[76] J. Heyd, G. E. Scuseria, and M. Ernzerhof, J. Chem. Phys. **118**, 8207 (2003).

[77] M. Schlipf and F. Gygi, Comput. Phys. Commun. **196**, 36 (2015).

[78] M. J. van Setten, M. Giantomassi, E. Bousquet, M. J. Verstraete, D. R. Hamann, X. Gonze, and G.-M. Rignanese, Comput. Phys. Commun. **226**, 39 (2018).

[79] L. Hedin, Phys. Rev. **139**, A796 (1965).

[80] C. A. Rozzi, D. Varsano, A. Marini, E. K. U. Gross, and A. Rubio, Phys. Rev. B **73**, 205119 (2006).

[81] G. Onida, L. Reining, and A. Rubio, Rev. Mod. Phys. **74**, 601 (2002).

[82] M. Rohlfing and S. G. Louie, Phys. Rev. B **62**, 4927 (2000).

[83] A. Marini, C. Hogan, M. Grüning, and D. Varsano, Comput. Phys. Commun. **180**, 1392 (2009).

[84] R. F. W. Bader, Acc. Chem. Res. **18**, 9 (1985).

[85] See Supplemental Material at http://link.aps.org/supplemental/10.1103/PhysRevB.108.165403 for details regarding the electronic band structures of monolayers C6N6 and B6O6, and their AA and AB stacking bilayers, strain energy per area concerning applied strain for AC-stacked C6N6/B6O6 heterostructure, valence band maximum (VBM) and conduction band minimum (CBM) of monolayers under compressive and tensile strains, as well as the effects of biaxial strain on the electronic band gap.

[86] S. Sarikurt and F. Ersan, Marmara Fen Bilimleri Derg. **30**, 383 (2018).

[87] R. Zhang, B. Li, and J. Yang, Nanoscale **7**, 14062 (2015).

[88] O. V. Yazyev, Rep. Prog. Phys. **73**, 056501 (2010).

[89] L.-p. Feng, J. Su, and Z.-t. Liu, J. Alloys Compd. **613**, 122 (2014).

[90] I. A. Moses and V. Barone, RSC Adv. **11**, 5773 (2021).

[91] M. Dogan, S. M. Gilbert, T. Pham, B. Shevitski, P. Ercius, S. Aloni, A. Zettl, and M. L. Cohen, Appl. Phys. Lett. **117**, 023102 (2020).

[92] S. E. Tsoeu, F. Opoku, and P. P. Govender, SN Appl. Sci. **2**, 341 (2020).

[93] X.-H. Li, B.-J. Wang, G.-D. Wang, X.-F. Yang, R.-Q. Zhao, X.-T. Jia, and S.-H. Ke, Sustainable Energy Fuels **5**, 2249 (2021).

[94] F. Ferreira and R. M. Ribeiro, Phys. Rev. B **96**, 115431 (2017).

[95] F. Karlicky and M. Otyepka, J. Chem. Theory Comput. **9**, 4155 (2013).

[96] M. Kolos, L. Cigarini, R. Verma, F. Karlicky, and S. Bhattacharya, J. Phys. Chem. C **125**, 12738 (2021).

[97] H. Mishra and S. Bhattacharya, Phys. Rev. B **99**, 165201 (2019).

[98] J. Sun, R. Zhang, X. Li, and J. Yang, Appl. Phys. Lett. **109**, 133108 (2016).

[99] Y. Zhang, C.-H. Hu, Y.-H. Wen, S.-Q. Wu, and Z.-Z. Zhu, New J. Phys. **13**, 063047 (2011).

[100] Y. Z. Abdullahi, T. L. Yoon, M. M. Halim, M. R. Hashim, and T. L. Lim, Philos. Mag. **97**, 2077 (2017).

[101] N. R. Abdullah, H. O. Rashid, C.-S. Tang, A. Manolescu, and V. Gudmundsson, J. Phys. Chem. Solids **155**, 110095 (2021).